0022-3565/10/3323-698–709$20.00
THE JOURNAL OF PHARMACOLOGY AND EXPERIMENTAL THERAPEUTICS
JPET 332:698–709, 2010

Vol. 332, No. 3
161802/3564860
Printed in U.S.A.

Antillatoxin, a Novel Lipopeptide, Enhances Neurite Outgrowth in Immature Cerebrocortical Neurons through Activation of Voltage-Gated Sodium Channels[S]

S. V. Jabba, A. Prakash, S. M. Dravid, W. H. Gerwick, and T. F. Murray

Department of Pharmacology, Creighton University School of Medicine, Omaha, Nebraska (S.V.J., A.P., S.M.D., T.F.M.); Department of Biotechnology, School of Bioscience and Biotechnology, Babasaheb Bhimrao Ambedkar University, Lucknow, India (A.P.); and Center for Marine Biotechnology and Biomedicine, Scripps Institution of Oceanography, and Skaggs School of Pharmacy and Pharmaceutical Sciences, University of California San Diego, La Jolla, California (W.H.G.)

Received September 21, 2009; accepted December 18, 2009

ABSTRACT

Antillatoxin (ATX) is a structurally novel lipopeptide that activates voltage-gated sodium channels (VGSC) leading to sodium influx in cerebellar granule neurons and cerebrocortical neurons 8 to 9 days in vitro (Li et al., 2001; Cao et al., 2008). However, the precise recognition site for ATX on the VGSC remains to be defined. Inasmuch as elevation of intracellular sodium ($[Na^+]_i$) may increase *N*-methyl-D-aspartate receptor (NMDAR)-mediated Ca^{2+} influx, Na^+ may function as a signaling molecule. We hypothesized that ATX may enhance neurite outgrowth in cerebrocortical neurons by elevating $[Na^+]_i$ and augmenting NMDAR function. ATX (30–100 nM) robustly stimulated neurite outgrowth, and this enhancement was sensitive to the VGSC antagonist, tetrodotoxin. To unambiguously demonstrate the enhancement of NMDA receptor function by ATX, we recorded single-channel currents from cell-attached patches. ATX was found to increase the open probability of NMDA receptors. Na^+-dependent up-regulation of NMDAR function has been shown to be regulated by Src family kinase (SFK) (Yu and Salter, 1998). The Src kinase inhibitor PP2 abrogated ATX-enhanced neurite outgrowth, suggesting a SFK involvement in this response. ATX-enhanced neurite outgrowth was also inhibited by the NMDAR antagonist, (5*R*,10*S*)-(+)-5-methyl-10,11-dihydro-5*H*-dibenzo[*a,d*]cyclohepten-5,10-imine hydrogen maleate (MK-801), and the calmodulin-dependent kinase kinase (CaMKK) inhibitor, 1,8-naphthoylene benzimidazole-3-carboxylic acid (STO-609), demonstrating the requirement for NMDAR activation with subsequent downstream engagement of the Ca^{2+}-dependent CaMKK pathway. These results with the structurally and mechanistically novel natural product, ATX, confirm and generalize our earlier results with a neurotoxin site 5 ligand. These data suggest that VGSC activators may represent a novel pharmacological strategy to regulate neuronal plasticity through NMDAR-dependent mechanisms.

This work was supported in part by the National Institutes of Health National Institute of Neurological Disorders and Stroke [Grant NS053398] (to W.H.G. and T.F.M.); and the National Institutes of Health National Center for Research Resources [Grant G20-RR024001].

Parts of this work were previously presented as follows: Jabba S, Gerwick WH, and Murray TF (2008) Antillatoxin, a novel lipopeptide, enhances neurite outgrowth in immature cerebrocortical neurons through activation of voltage-gated sodium channels. *2008 Neuroscience Meeting*; 2008; Nov 15–19; Washington, DC. Program no. 807.2, Society for Neuroscience, Washington, DC.

Article, publication date, and citation information can be found at http://jpet.aspetjournals.org.

doi:10.1124/jpet.109.161802.

[S] The online version of this article (available at http://jpet.aspetjournals.org) contains supplemental material.

Antillatoxin (ATX) is a structurally novel lipopeptide with an exceptionally high degree of methylation unlike any known natural product (Lee and Loh, 2006). Isolated from the cyanobacterium *Lyngbya majuscula*, this compound is also distinguished by multiple stereocenters (Orjala et al., 1995). The essential role of the asymmetric carbon atoms in ATX is reflected in the stereoselective effects of ATX enantiomers (Li et al., 2004). ATX is considered to be the second most potent ichthyotoxic compound obtained from marine sources after only brevetoxin (PbTx)-1 (Orjala et al., 1995). Exposure to *L. majuscula* blooms are associated with adverse

ABBREVIATIONS: ATX, antillatoxin; PbTx, brevetoxin; VGSC, voltage-gated sodium channel; $[Na^+]_i$, intracellular Na^+ concentration; NMDAR, *N*-methyl-D-aspartate receptor; SFK, Src family kinase; VGCC, voltage-gated Ca^{2+} channel; CaMK, Ca^{2+}/calmodulin-dependent protein kinase; MAPK, mitogen-activated protein kinase; CaMKK, CaMK kinase; TTX, tetrodotoxin; MK-801, (5*R*,10*S*)-(+)-5-methyl-10,11-dihydro-5*H*-dibenzo-[*a,d*]cyclohepten-5,10-imine hydrogen maleate; STO-609, 1,8-naphthoylene benzimidazole-3-carboxylic acid; PP2, 4-amino-5-(4-chlorophenyl)-7-(*t*-butyl)pyrazolo[3,4-*d*] pyrimidine; PP3, 4-amino-7-phenylpyrazol [3,4-*d*] pyrimidine; PBS, phosphate-buffered saline; PGP 9.5, protein gene product 9.5; DIV, days in vitro; PVP, polyvinylpyrrolidone; SBFI, sodium-binding benzofuran isophthalate; FMP, FLIPR membrane potential; CI, confidence interval; E_M, estimation of membrane potential; P_o, open probability.

human health effects, including respiratory irritation, eye inflammation, and severe contact dermatitis. Previous work has demonstrated that ATX is a potent activator of voltage-gated sodium channels (VGSCs) that elevates intracellular Na^+ concentration ($[Na^+]_i$) in intact neurons (Li et al., 2001; Cao et al., 2008). Moreover, ATX has been shown to be neurotoxic in cerebellar granule cells through an indirect activation of *N*-methyl-D-aspartate receptors (NMDARs) as a consequence of glutamate release (Li et al., 2001, 2004).

Regulation of $[Na^+]_i$ plays a critical role in the nervous system, not only because Na^+ influx through VGSCs is responsible for the initiation and propagation of action potentials but also because various neuronal cell functions, such as intracellular pH, Ca^{2+} homeostasis, and reuptake of neurotransmitters, are dependent on the Na^+ gradient. Previous studies have further indicated that intracellular Na^+ can also act as a signaling molecule to modulate cell functions, such as cell proliferation, ion channel permeability, G-protein function, and opioid ligand-receptor interactions (Yu, 2006). Moreover, recent studies have demonstrated that neuronal activity-mediated increases in $[Na^+]_i$ in structures, including soma, dendrites, and spines, may act as a signaling molecule and contribute to activity-dependent synaptic plasticity (Rose and Konnerth, 2001). In cerebellar Purkinje neurons, α-amino-3-hydroxy-5-methyl-4-isoxazolepropionic acid receptor-mediated Na^+ influx was shown to be required for induction of long-term depression (Linden et al., 1993). In both hippocampal and immature cerebrocortical neurons, an elevation in intracellular Na^+ was found to increase NMDAR-mediated whole-cell currents and NMDAR single-channel activity by increasing both channel open probability and mean open time (Yu and Salter, 1998; George et al., 2009). This $[Na^+]_i$-mediated up-regulation of NMDAR function has been shown to require Src kinase activation (Yu and Salter, 1998; George et al., 2009). Src family kinases (SFKs) act as a crucial point of convergence for signaling pathways that enhance NMDAR activity, and, by up-regulating the function of NMDARs, Src gates the production of NMDAR-dependent synaptic potentiation and plasticity (Salter and Kalia, 2004).

Neuronal activity has a major role in the development of dendritic complexity and neuronal circuits. The mechanisms by which neuronal activity translate into morphological changes are complex. Numerous studies have shown that activity-dependent neuronal development involves various calcium influx pathways mediated by ionotropic glutamate receptors (NMDAR) and voltage-gated Ca^{2+} channels (VGCCs) (Ghosh and Greenberg, 1995; West et al., 2002). Intracellular calcium acts as a signaling molecule largely through the binding to calmodulin, a calcium-binding protein that engages downstream Ca^{2+}/calmodulin-dependent protein kinase (CaMK) and mitogen-activated protein kinase (MAPK) signaling pathways (Ghosh and Greenberg, 1995; West et al., 2002). CaMK kinase (CaMKK) has been demonstrated to be an upstream regulator of both CaMK- and MAPK-signaling pathways. Moreover, previous studies have demonstrated that activity-dependent neurite outgrowth (Wayman et al., 2006) and synaptogenesis (Saneyoshi et al., 2008) are regulated by NMDAR-dependent CaMKK/calmodulin kinase I-signaling cascades. Therefore, NMDARs play a critical role in activity-dependent development and plasticity (Ghosh and Greenberg, 1995), dendritic arborization (Wong and Ghosh, 2002; Miller and Kaplan, 2003; Wayman et al., 2006), spine morphogenesis (Ultanir et al., 2007), and synapse formation (Saneyoshi et al., 2008) by stimulating these calcium-dependent signaling pathways.

Inasmuch as neuronal activity-induced increments in cytoplasmic sodium may augment NMDAR-mediated currents, we reasoned that intracellular Na^+ may function as a signaling molecule and regulate neuritogenesis in immature cerebrocortical neurons. We recently demonstrated that PbTx-2, a VGSC activator, enhanced NMDAR function and augmented neurite outgrowth (George et al., 2009). In the present study, we extend our earlier work to demonstrate that these pharmacologic actions of the neurotoxin site 5 ligand, brevetoxin, generalize to the structurally and mechanistically novel VGSC activator ATX. We found that ATX promoted neuritogenesis by elevating $[Na^+]_i$, which in turn augmented NMDAR function leading to Ca^{2+} influx and engagement of a CaMKK pathway. These data provide further support for the hypothesis that sodium channel activators seem to be capable of mimicking activity-dependent neuronal development through potentiation of NMDAR signaling pathways that influence neuronal plasticity.

Materials and Methods

Cerebrocortical Neuron Culture. Primary cultures of cerebrocortical neurons were harvested from Swiss Webster mice on embryonic day 16 and cultured as described previously (Cao et al., 2008). Cells were plated onto poly-L-lysine-coated (Sigma-Aldrich, St. Louis, MO) 96-well (9 mm), clear-bottomed, black-well culture plates (Corning Life Sciences, Lowell, MA) at a density of 1.8×10^6 cells/ml (150 μl/well), 24-well (15.6 mm) culture plates at a density of 0.05×10^6 cells/ml (0.5 ml/well), or 6-well (35 mm) culture dishes at a density of 2.25×10^6 cells/ml (2 ml/well), respectively, and incubated at 37°C in a 5% CO_2 and 95% humid atmosphere. All animal use protocols were approved by the Creighton University Institutional Animal Care and Use Committee.

Immunocytochemistry and Determination of Total Neurite Length. Cells were plated on poly-lysine-coated 12- or 15-mm glass coverslips (Thermo Fisher Scientific, Waltham, MA) and placed inside of 24-well culture plates at a low density of 0.05×10^6 cells/ml (0.5 ml/well). To assess the influence of ATX on neuritogenesis, primary cultures of immature cerebrocortical neurons were exposed to various concentrations of ATX ranging from 1 to 1000 nM for 24 h beginning 3 h after plating, and total neurite outgrowth was measured. In some experiments, these concentrations of ATX were coincubated with tetrodotoxin (TTX; 1 μM) (BIOMOL Research Laboratories, Plymouth Meeting, PA), MK-801 (1 μM) (Sigma-Aldrich), nifedipine (1 μM) (Sigma-Aldrich), STO-609 (2.6 μM) (Calbiochem, San Diego, CA), PP2, or PP3 (Calbiochem). At 24 h after plating, cultures were fixed at room temperature for 20 min using 4% paraformaldehyde in phosphate-buffered saline (PBS). After fixation, neurons were blocked and permeabilized by incubating for 30 min with PBS containing 2% fetal bovine serum (Atlanta Biologicals, Lawrenceville, GA) and 0.15% Triton X-100 (Sigma-Aldrich). The coverslips were incubated overnight at 4°C with protein gene product 9.5 (anti-PGP 9.5) primary antibody (AbD SeroTec, Raleigh, NC). After washing three times in blocking buffer, coverslips were incubated with a secondary antibody [fluorescein isothiocyanate (anti-rabbit IgG)] (Jackson ImmunoResearch Laboratories Inc., West Grove, PA) for 60 min at room temperature. Coverslips were washed and mounted on microscope slides and analyzed by fluorescence microscopy on an Olympus IX 71 inverted microscope with a Nikon camera. Digital images of individual neurons were captured, and total neurite length was quantified using Image-Pro plus (Media Cybernetics, Inc., Bethesda, MD). To reduce the effect of paracrine neurotrophic factors on neurite growth, only those neurons that were

separated from surrounding cells by approximately 150 μm were digitally acquired and analyzed. Digital images of individual neurons were captured and exported as 8-bit images. All neurites in a single neuron including those from secondary branches were manually traced, and the length was measured by using the "Create Trace" option of measurement module of Image-Pro Plus software (Media-Cybernetics, Inc.). Total neurite length was calculated by adding all the neurite lengths traced and measured on individual neurons. At least 25 randomly chosen neurons from two different cultures were evaluated for each treatment group.

Diolistic Labeling. The Helios Gene Gun System (Bio-Rad Laboratories, Hercules, CA) was used to deliver DiI-coated tungsten particles (1.3 μM) (Bio-Rad Laboratories) into paraformaldehyde-fixed cerebrocortical neurons 1 day in vitro (DIV). Diolistic bullet preparation was based on the method of O'Brien and Lummis (2006). In brief, 2.5 to 3.5 mg of DiI (Invitrogen, Carlsbad, CA) was suspended in 200 μl of dichloromethane (Sigma-Aldrich). The dissolved dye was added over evenly spread tungsten particles (35 mg) placed on a clean glass slide and then allowed to dry. The dye-coated particles were scraped onto another clean glass slide and chopped to fine particles using a clean razor blade and later resuspended in 3 ml of deionized water. This dye slurry was sonicated for 10 min and then vortex briefly to form a uniform suspension. After adding 100 μl of polyvinylpyrrolidone (PVP) (Bio-Rad Laboratories) stock solution (0.96% PVP in ethanol) to the dye slurry, it was drawn into a PVP-precoated Tefzel tubing mounted on a preparation station (Bio-Rad Laboratories) using a 5- to 10-ml syringe. The dye particles were allowed to settle for 20 to 30 min, and then the supernatant water was carefully withdrawn from Tefzel tubing (Bio-Rad Laboratories) using a syringe. The tubing was rotated for 1 to 2 min to uniformly spread the particles. The tubing was then allowed to dry for 5 min before cutting into bullets using a tube cutter. The DIV-1 cerebrocortical neurons grown on coverslips were shot postfixation (1.5% paraformaldehyde) using DiI bullets loaded onto a Helios gene gun at 140 to 160 psi of helium pressure from a distance of 2.5 cm. The dye particles were allowed to spread across the neuronal membrane overnight, and coverslips were then mounted for imaging.

Intracellular Sodium Concentration Measurement. $[Na^+]_i$ measurement and full in situ calibration of sodium-binding benzofuran isophthalate (SBFI) fluorescence ratio were performed as described previously (Cao et al., 2008). Cells grown in 96-well plates were washed four times with Locke's buffer (8.6 mM HEPES, 5.6 mM KCl, 154 mM NaCl, 5.6 mM glucose, 1.0 mM $MgCl_2$, 2.3 mM $CaCl_2$, 0.1 mM glycine, pH 7.4) using an automated microplate washer (BioTek Instruments, Winooski, VT). After measuring the background fluorescence of each well, cells were incubated for 1 h at 37°C with dye-loading buffer (100 μl/well) containing 10 μM SBFI-AM (Invitrogen) and 0.02% Pluronic F-127 (Invitrogen). Cells were then washed five times with Locke's buffer, leaving a final volume of 120 μl in each well. The plate was then transferred back to the incubator for 15 min to allow the cells to equilibrate after washing and then placed in a FlexStation II (Molecular Devices, Sunnyvale, CA) chamber to detect Na^+-bound SBFI emission at 505 nm (cells were excited at 340 and 380 nm). Fluorescence readings were taken once every 5 s for 60 s to establish the baseline, and then 40 μl of ATX was added to each well from the compound plate at a rate of 26 μl/s, yielding a final volume of 160 μl/well. After correcting for background fluorescence, SBFI fluorescence ratios (340/380) versus time were analyzed, and time- or concentration-response graphs were generated using GraphPad Prism (GraphPad Software Inc., San Diego, CA).

Full in situ calibration of the SBFI fluorescence ratio was performed using calibration media containing the following: 0.6 mM $MgCl_2$, 0.5 mM $CaCl_2$, 10 mM HEPES, Na^+ and K^+ such that $[Na^+]$ plus $[K^+] = 130$, 100 gluconate, and 30 Cl^- (titrated with 10 mol/l KOH to pH 7.4). Gramicidin D (5 μM) (Na^+ ionophore) (Invitrogen), monensin (10 μM) (Na^+/H^+ carrier), and ouabain (100 μM) (Na^+/K^+-ATPase inhibitor) (Calbiochem) to equilibrate the intracellular and extracellular sodium concentration. After five washes, Locke's buffer was replaced by 150 μl of sodium-containing calibration solution (0–130 mM). The plate was then loaded onto the FlexStation chamber for recording of emitted fluorescence during excitation at 340 and 380 nm. Fluorescence data were converted to a ratio (340/380) after background correction. To convert the fluorescence ratio of emitted SBFI signals into a $[Na^+]_i$ value, the following equation was used: $[Na^+] = \beta K_d [(R - R_{min})/(R_{max} - R)]$ (eq. 1), where β is the ratio of the fluorescence of the free (unbound) dye to bound dye at the second excitation wavelength (380 nm), K_d is the apparent dissociation constant of SBFI for Na^+, R is the background-subtracted SBFI fluorescence ratio, and R_{min} and R_{max} are the minimum and maximum fluorescence values, respectively. Data relating $[Na^+]_i$ to R were fitted by a three-parameter hyperbolic equation having the following form: $R = R_{min} + [a ([Na^+])/(b + [Na^+])]$ (eq. 2), where a and b are constants and equal to $R_{max} - R_{min}$ and βK_d, respectively. These data relating $[Na^+]_i$ to R (see Fig. 6B) were well described ($r^2 = 0.98$) by eq. 2. The derived parameters were $R_{min} = 1.47 \pm 0.03$, $a = 3.541 \pm 0.11$, and $b = 63.30 \pm 4.93$. The value for R_{min} obtained by this method was similar to the value of R_{min} derived experimentally at $[Na^+] = 0$ mM. Therefore, the corresponding values for R_{max} and βK_d were $R_{max} = 5.01 \pm 0.13$ and $\beta K_d = 63.30 \pm 4.93$ mM. We compared the values of R_{max} and βK_d obtained from a Hanes plot (Cao et al., 2008) to those derived from the three-parameter hyperbolic fit. The equation was rearranged to generate a Hanes plot such that $[Na^+]/(R - R_{min}) = \{[Na^+]/(R_{max} - R_{min})\} + [\beta K_d/(R_{max} - R_{min})]$ (eq. 3).

The plotting of $[Na^+]/(R - R_{min})$ versus $[Na^+]_i$ as a Hanes function yielded a straight line ($r^2 = 1$) (data not shown). The slope $\{1/(R_{max} - R_{min})\}$ of this regression provides a means to estimate of R_{max}, whereas the intercept on the abscissa is equal to $-\beta K_d$. The value for R_{min} was obtained from the experimental data. The values of R_{max} and βK_d calculated from Hanes plot were 4.97 ± 0.10 and 63.3 ± 1.9 mM, respectively, and were therefore not significantly different from the values derived from the three-parameter hyperbolic fit, which were 5.01 ± 0.13 (R_{max}) and 63.3 ± 4.93 mM (βK_d).

Intracellular Ca^{2+} Monitoring. DIV-1 cerebrocortical neurons grown in 96-well plates were used for intracellular Ca^{2+} concentration ($[Ca^{2+}]_i$) measurements as described previously (George et al., 2009). In brief, the growth medium was removed and replaced with dye-loading medium (100 μl/well) containing 8 μM fluo-3 AM (Invitrogen) and 0.04% Pluronic acid in Locke's buffer. After 1-h incubation in dye-loading medium, the neurons were washed four times in fresh Locke's buffer (200 μl/well, 22°C) using an automated microplate washer (BioTek Instruments) and transferred to a FlexStation II benchtop scanning fluorometer chamber. The final volume of Locke's buffer in each well was 120 μl. Fluorescence measurements were performed at 37°C. The neurons were excited at 488 nm, and Ca^{2+}-bound fluo-3 emission was recorded at 538 nm at 1.2-s intervals. After recording baseline fluorescence for 27 s, 40 μl of a 4× concentration of ATX in the presence or absence of either PP2, PP3, nifedipine, or MK-801 were added to the cells at a rate of 26 μl/s, yielding a final volume of 160 μl/well; the fluorescence was monitored for an additional 220 to 270 s. The fluo-3 fluorescence was expressed as $(F_{max} - F_{min})/F_{min}$, where F_{max} is the maximum and F_{min} is the minimum fluorescence measured in each well.

Western Blotting. Western blot analysis was performed by using cells grown in six-well plates. Three hours after plating, cells were exposed to 30 nM ATX for time periods ranging from 0 to 24 h at 37°C. At the end of each time period, cultures were transferred onto an ice slurry to terminate drug exposure and washed three times with ice-cold PBS. Cells were lysed using ice-cold lysis buffer (50 mM Tris, 50 mM NaCl, 2 mM EDTA, 2 mM EGTA, 1% Nonidet P40, 0.1% SDS, 2.5 mM sodium pyrophosphate, and 1 mM sodium orthovanadate). Phenylmethylsulfonyl fluoride (1 mM) and 1× protease inhibitor mixture (Sigma-Aldrich) were then added, and the lysate was incubated for 30 min at 4°C. Cell lysates were sonicated and then centrifuged at 13,000*g* for 15 min at 4°C. The supernatant was assayed by the Bradford method (Bradford, 1976) to determine pro-

tein content. Equal amounts of protein were mixed with the Laemmli sample buffer and heated for 5 min at 75°C. The samples were loaded onto a 10% SDS-polyacrylamide gel electrophoresis gel and transferred to a nitrocellulose membrane and immunoblotted with anti-phospho-Src (416) and total Src antibodies (Cell Signaling Technology Inc., Danvers, MA). Blots were developed with ECL Plus kit (GE Healthcare, Chalfont St. Giles, UK) for 3 min. Blots were subsequently stripped (63 mM Tris base, 70 mM SDS, 0.0007% 2-mercaptoethanol, pH 6.8) and reprobed for further use. Western blot densitometry data were obtained by using MCID Basic 7.0 software (Imaging Research, St. Catharines, ON, Canada).

Membrane Potential Assay Fluorescence Monitoring. Membrane potential in the cerebrocortical neuron cultures was determined by using the FLIPR membrane potential (FMP) assay (Molecular Devices) as described previously (George et al., 2009). FMP blue dye was used to assess the membrane potential of neurons in culture. Quantification of changes in membrane potential was derived using KCl as a reference. In preliminary experiments, we determined that, with cerebrocortical neurons in culture, the optimal dye concentration was one-eighth of that suggested by the manufacturer. After removing the culture medium, 180 μl of assay buffer was added to the neurons, and the plate was incubated at 37°C in a 5% CO_2 and 95% humid atmosphere for 30 min. For KCl calibration measurements, varying concentrations of 10× KCl standard solutions in assay buffer were prepared. After 30-min equilibration incubation, the plate was transferred to a FlexStation II chamber, and the fluorescence measurements were performed at 37°C. Neurons were excited at 530 nm, and emission was recorded at 565 nm at 2-s intervals. After recording the baseline for 60 s, either 20 μl of KCl or ATX was added to a final volume of 200 μl at a rate of 26 μl/s, and the fluorescence was monitored for an additional 240 s.

A linear regression analysis of the log $[K^+]$ versus FMP blue fluorescence change ($F - F_0$) was generated. We used the Goldman-Hodgkin-Katz equation to generate a standard curve for the estimation of membrane potential (E_M) at various concentrations of extracellular K^+:

$$E_{m,K,Na,Cl} = \frac{RT}{F} \ln \left(\frac{P_{Na^+}[Na^+]_{out} + P_{K^+}[K^+]_{out} + P_{Cl^-}[Cl^-]_{in}}{P_{Na^+}[Na^+]_{in} + P_{K^+}[K^+]_{in} + P_{Cl^-}[Cl^-]_{out}} \right)$$

where E_M is membrane potential, R is universal gas constant, T is temperature using the Kelvin scale, F is faraday constant, and P_K, P_{Na}, and P_{Cl} are relative permeabilities for K^+, Na^+, and Cl^-, respectively. $[K^+]_{out}$, $[Na^+]_{out}$, and $[Cl^-]_{out}$, and $[K^+]_{in}$, $[Na^+]_{in}$, and $[Cl^-]_{in}$ are the respective extracellular and intracellular concentrations of K^+, Na^+, and Cl^-. A DIV-1 neuronal $[Cl^-]_{in}$ value of 140 mM was used for these calculations. The regression for the $[K^+]_{out}$ versus Δfluorescence and E_M was used for estimating ATX-induced change in membrane potential.

Electrophysiology. Single-channel currents were recorded at 23°C in the cell-attached configuration. Patch pipettes were pulled from borosilicate glass capillaries (Warner Instruments, Hamden, CT), coated with Sylgard 184 (Dow Corning, Midland, MI), and fire-polished to a resistance of 10 to 15 MΩ when filled with the pipette solution. The external recording solution consisted of Mg^{2+}-free Locke's buffer with 20 μM EDTA to chelate trace amounts of divalent cations. ATX was always bath-applied. The patch pipette solution consisted of extracellular Locke's buffer without $MgCl_2$ and with 100 μM NMDA and 100 μM glycine. In some experiments, 10 μM strychnine, 10 μM bicuculline methiodide, and 10 μM 6,7-dinitroquinoxalinedione were included in the external solution to block nonspecific components. All recordings were done from DIV-1 cerebrocortical neurons. Cell-attached patch recordings were done using an Axopatch 200B amplifier (Molecular Devices), filtered at 8 kHz (−3 dB, 8-pole Bessel), and digitized at 40 kHz with Axon pClamp 10.2 software (Molecular Devices). The pipette potential was +60 mV. Records were idealized with a segmental k-means algorithm using QUB software (www.qub.buffalo.edu). All conductance levels were assumed to be equal for the analysis. Dwell-time histograms were generated and fitted using Channelab (Synaptosoft, Decatur, GA) with an imposed dead time of 50 μs. The open probability (P_o), mean open time, and amplitude were compared by paired t test. For representation in figures, the P_o and mean open time were normalized to the average of respective control values. The corresponding ATX-treated values were normalized to their paired control values.

Resting membrane potential was measured by recording unitary NMDA receptor currents in cell-attached mode at different pipette potentials as described previously (Tyzio et al., 2003). Under conditions where NMDA receptors exhibit linear current-voltage relationships and reverse at 0 mV, the expected membrane potential of the cell will be equal to the pipette potential at which the NMDA channel reverses in cell-attached mode.

Results

Antillatoxin Is a VGSC Activator in Immature Cerebrocortical Neurons. In previous reports, we demonstrated that ATX is an activator of VGSCs in cerebellar granule neurons (Li et al., 2001) and mature (DIV-9) cerebrocortical neurons (Cao et al., 2008). Therefore, we sought to determine whether immature cerebrocortical neurons were also sensitive to ATX-induced elevation of $[Na^+]_i$. We assessed ATX-induced elevation of $[Na^+]_i$ in DIV-1 cerebrocortical neurons loaded with SBFI. As shown in Fig. 1, A and B, 30 nM ATX elevated $[Na^+]_i$ in DIV-1 cerebrocortical neurons (***, $p <$

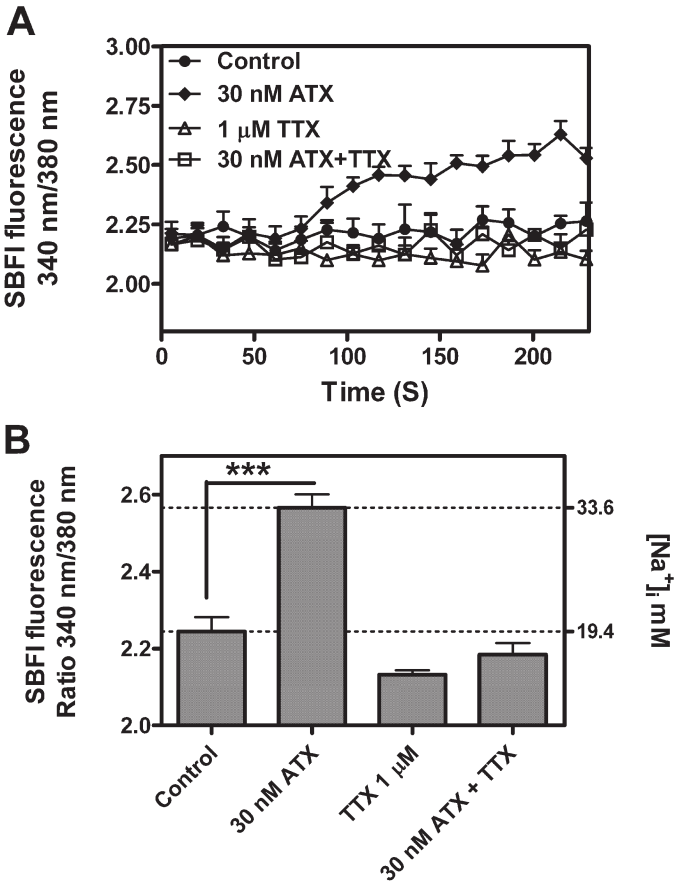

Fig. 1. ATX increases intracellular sodium levels in DIV-1 cerebrocortical neurons. A, time-response curve for ATX stimulation of Na^+ influx. This ATX-induced stimulation of Na^+ influx was prevented by coapplication of 1 μM TTX. B, histogram representing SBFI fluorescence ratio (340/380) values after the indicated treatments. Data shown are from an experiment performed in octuplicates. ***, $p < 0.001$, unpaired t test.

0.001). To confirm that the observed Na^+ influx was mediated by VGSCs, we tested the influence of TTX, a selective antagonist of VGSCs, on the response to ATX. Pretreatment of DIV-1 cerebrocortical neurons with TTX (1 μM) abolished ATX-induced Na^+ influx. These results indicate that ATX is an activator of VGSCs in DIV-1 cerebrocortical neurons.

Antillatoxin Enhances Neurite Outgrowth in Immature Cerebrocortical Neurons. We next wanted to determine the influence of ATX on neuritogenesis in immature cerebrocortical neurons. Three hours after plating, primary cultures of immature cerebrocortical neurons were exposed to various concentrations of ATX ranging from 1 to 1000 nM for 24 h, and total neurite outgrowth was then assessed. Either immunostaining of PGP 9.5 or diolistic labeling was used to visualize neurons and determine the influence of ATX on neurite outgrowth (Fig. 2A). ATX significantly enhanced total neurite outgrowth in immature cerebrocortical neurons with concentrations of 30 and 100 nM producing a robust >2-fold increase in total neurite length (***, $p < 0.001$) (Fig. 2B; Supplemental Fig. 1). As previously observed with PbTx-2, the ATX concentration-response profile was bidirectional, or hormetic (Fig. 2B).

Antillatoxin-Induced Neurite Outgrowth Is Mediated by VGSCs. Given that ATX is a VGSC activator with the ability to augment neurite outgrowth, we wanted to confirm the involvement of VGSCs in the latter functional response. DIV-1 cerebrocortical neurons were coincubated in the presence or absence of TTX (1 μM) and 30 nM ATX for 24 h, and total neurite length was determined. Consistent with the involvement of VGSCs, TTX completely abolished ATX-induced neurite outgrowth (control, 109.5 ± 22.5 μm; TTX, 153.23 ± 8.4 μm; ATX, 236.65 ± 17.9 μm; TTX plus ATX, 115.3 ± 11.8 μm, *, $p < 0.05$) (Fig. 3, A and B).

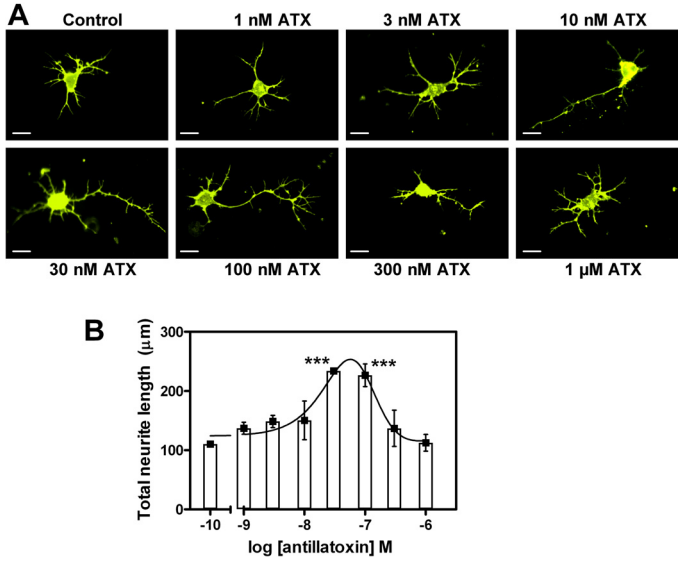

Fig. 2. Effect of ATX on neurite outgrowth. A, representative images of DiI-loaded immature cerebrocortical neurons at 24 h after plating (scale bar, 10 μm). Various concentrations of ATX were added to the culture medium at 3 h after plating. Depicted neurons were visualized by diolistic loading with DiI. B, quantification of concentration-response effects of ATX on neurite outgrowth at 24 h after plating. ATX-enhanced neurite outgrowth displayed a hormetic concentration-response relationship with maximal enhancement seen at 30 to 100 nM ATX. Quantification of total neurite length was performed with Image Pro Plus. The experiment was performed twice, and each point represents the mean value derived from analysis of 25 to 30 neurons. ***, $p < 0.001$, unpaired t test.

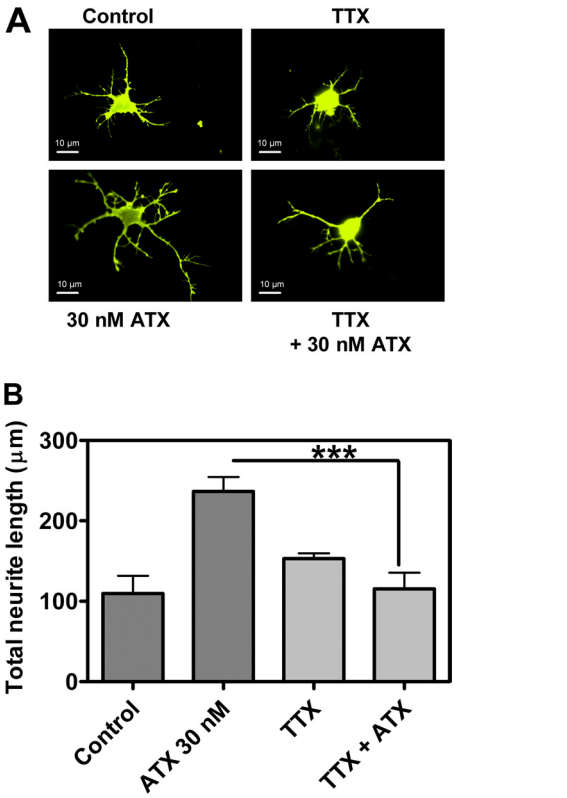

Fig. 3. Effect of TTX on ATX-induced neurite outgrowth in immature cerebrocortical neurons. A, representative images (scale bar, 10 μm) and (B) quantification of the effects of TTX on ATX-enhanced neurite outgrowth at 24 h after plating. Neurons were treated with 30 nM ATX in the presence and absence of 1 μM TTX beginning at 3 h after plating. The experiment was repeated twice, and 25 to 30 neurons were quantified for each exposure condition. ***, $p < 0.05$, unpaired t test.

Antillatoxin-Induced Neurite Outgrowth Involves NMDARs, VGCCs, and the Ca^{2+}-Dependent CaMKK Pathway. Inasmuch as previous studies have indicated that activity-dependent neuritogenesis and neuronal development involve Ca^{2+} influx pathways through NMDAR and VGCCs with subsequent engagement of a CaMKK pathway (Konur and Ghosh, 2005; Wayman et al., 2006), we assessed the role of this signaling cascade in ATX-induced neurite outgrowth. Coincubation of MK-801 (1 μM), an uncompetitive blocker of NMDAR with 30 nM ATX, abrogated ATX-enhanced neurite outgrowth in immature cerebrocortical neurons (Fig. 4, A and B) (control, 109.5 ± 22.5 μm; ATX, 236.65 ± 17.9 μm; ATX plus MK-801, 113.8 ± 9.8 μm, ***, $p < 0.001$), demonstrating that ATX-enhanced neurite outgrowth involves NMDARs. To investigate the role of VGCCs in the response to ATX, we used the L-type calcium channel blocker, nifedipine (1 μM). Nifedipine pretreatment partially reduced ATX-stimulated neurite outgrowth (Fig. 4, A and B) (control, 109.5 ± 22.5 μm; ATX, 236.65 ± 17.9 μm; ATX plus nifedipine, 166.3 ± 13.45 μm, *, $p < 0.05$), suggesting that VGCCs may play a role in the response to ATX. Next, we investigated the involvement of a downstream Ca^{2+}-dependent CaMKK in ATX-induced stimulation of neurite outgrowth. CaMKK is an important upstream activator of essential signaling mediators of activity-dependent neurite outgrowth, such as CaMK1, CaMKIV, and MAPKs. STO-609 (2.6 μM), a selective CaMKK inhibitor, eliminated the stimulatory effect of ATX on neurite outgrowth in immature

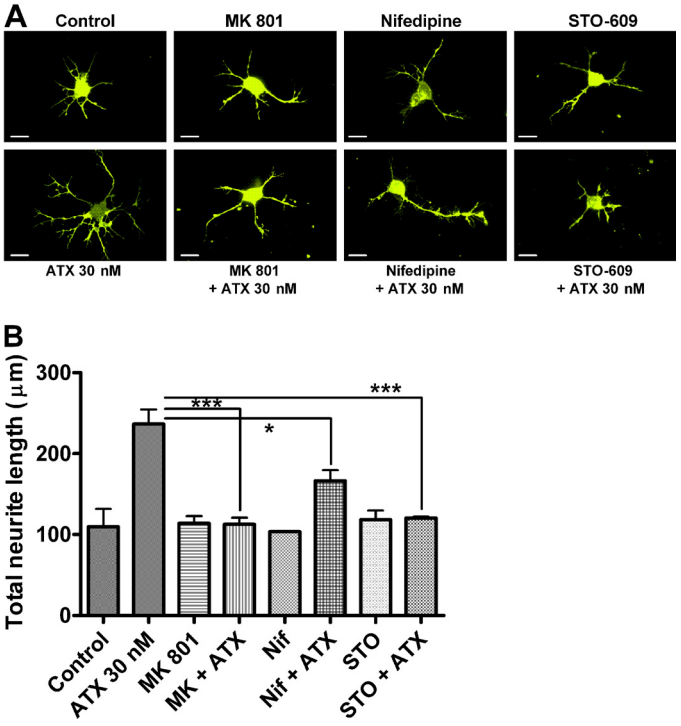

Fig. 4. Pharmacological evaluation of signaling pathways involved in ATX-enhanced neurite outgrowth. A, representative images (scale bar, 10 μm) and (B) quantification of neurite extension at 24 h. The 30 nM ATX exposure was examined in the presence or absence of MK-801 (1 μM), nifedipine (1 μM), or STO-609 (2.6 μM) beginning at 3 h after plating. The experiment was repeated twice, and 25 to 30 neurons were quantified for each exposure condition. ***, $p < 0.001$, *, $p < 0.05$, unpaired t test.

cerebrocortical neurons (Fig. 4, A and B) (control, 109.5 ± 22.5 μm; ATX, 236.65 ± 17.9 μm; ATX plus STO-609, 120.4 ± 9.02 μm, ***, $p < 0.001$). This observation suggests that a Ca^{2+}-dependent CaMKK pathway contributes to the stimulatory effects of ATX on neuritogenesis.

Antillatoxin-Induced Neurite Outgrowth Is Mediated by Src Family Tyrosine Kinase Activation. Activity-dependent neurite outgrowth involves up-regulation of NMDAR function. Because earlier studies (Yu et al., 1997; Yu and Salter, 1998; Salter and Kalia, 2004) have shown that $[Na^+]_i$ and activated SFKs up-regulate NMDAR function, we reasoned that SFKs may participate in ATX-enhanced neurite outgrowth. Exposure of neurons to the Src family kinase inhibitor PP2 (2 μM), but not its inactive congener PP3 (2 μM), eliminated the stimulatory effect of ATX on neurite outgrowth. These findings establish a role for Src family kinases in ATX-induced stimulation of neurite outgrowth (Fig. 5, A and B) (control, 118.8 ± 12.9 μm; ATX, 194.4 ± 17.2 μm; ATX plus PP2, 83.9 ± 9.7 μm; ATX plus PP3, 181.3 ± 15.3 μm). The catalytic activity of Src kinase is controlled by phosphorylation and dephosphorylation events, primarily that of Tyr416. Intermolecular autophosphorylation of Tyr416 stimulates Src kinase activity by permitting access to its substrates and ligands (Yu et al., 1997). To assess the ability of ATX to activate Src, we determined the phosphorylation of the Tyr416 residue by using an anti-phospho-Tyr416 Src antibody. Immature cerebrocortical neurons were exposed to 30 nM ATX, and cell lysates were collected at various time periods for Western blot analysis. These results revealed that 30 nM ATX produced a robust activation of

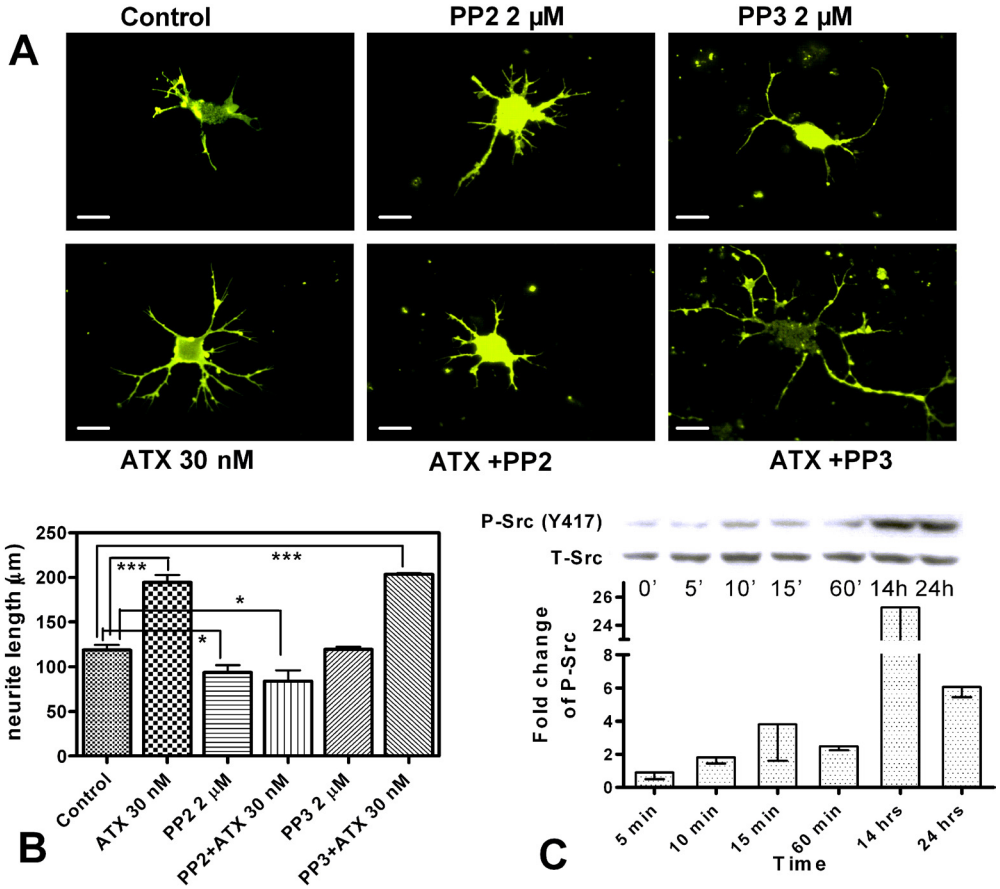

Fig. 5. ATX-induced neurite extension involves a Src family kinase. A, representative images (scale bar, 10 μm) and quantification of neurite extension at 24 h (B). Cerebrocortical neurons were treated with 30 nM ATX in the presence or absence of either 2 μM PP2 or PP3 beginning at 3 h after plating. The experiment was repeated four times, and 20 to 30 neurons were quantified for each exposure condition. ***, $p < 0.001$, *, $p < 0.05$, unpaired t test. C, tyrosine phosphorylation (Tyr416) of Src kinase determined by immunoblotting. Cerebrocortical neurons were treated with 30 nM ATX beginning at 3 h after plating, and P-Src (Tyr416) was assessed at the indicated times. A representative blot is shown. The experiment was performed twice with independent cultures. Also depicted is the quantitative analysis of the relative band densities of immunoblots. Each bar represents mean ± S.E.M. of two values.

Src kinase as reflected in the sustained increase in the phosphorylation of Tyr416 (Fig. 5, B and C). These findings indicate that ATX exposure produces an activation of Src kinase that is temporally correlated with the stimulation of neurite outgrowth.

Antillatoxin Increases Intracellular Sodium Levels in Immature Cerebrocortical Neurons. Given that the earlier studies of Yu and Salter (Yu et al., 1997; Yu and Salter, 1998; Yu, 2006) demonstrated that $[Na^+]_i$ is a regulator of NMDAR-mediated signaling, it was important to quantify the magnitude of ATX-induced elevation of $[Na^+]_i$ in immature cerebrocortical neurons. SBFI, a sodium-sensitive fluorescent indicator, was used to determine the influence of ATX on $[Na^+]_i$ in DIV-1 cerebrocortical neurons. Full in situ calibration was performed in DIV-1 cerebrocortical neurons to determine the relationship between the ratiometric SBFI signal and $[Na^+]_i$ (Cao et al., 2008; George et al., 2009). Cells loaded with the SBFI were excited at 340 and 380 nm, and the emitted fluorescence was recorded at 505 nm. The 340/380 emission ratio was calculated after background correction (Fig. 6A). A three-parameter hyperbolic function adequately fit the calibration data relating SBFI fluorescence ratio to $[Na^+]_i$ (Fig. 6B). ATX produced a concentration-dependent increase in $[Na^+]_i$ (Fig. 6C) with an EC_{50} value of 114.2 nM (70.8 to 184.2 nM, 95% CI). The in situ SBFI calibration showed that basal $[Na^+]_i$ in DIV-1 cerebrocortical neurons was 17.3 ± 0.37 mM and that ATX produced a maximal elevation of 78.6 ± 6.9 mM (Fig. 6D). Because a 30 nM concentration of ATX was sufficient to produce a robust increase in neurite outgrowth, it was important to quantify the $[Na^+]_i$ increment associated with this treatment. The 30 nM ATX treatment produced a maximal $[Na^+]_i$ of 26.1 ± 0.4 mM, representing an increment of 8.8 mM over basal. Previous reports in hippocampal neurons suggested that an increment of $[Na^+]_i$ of 10 mM was sufficient to produce significant increases in NMDAR channel activity (Yu and Salter, 1998; Yan et al., 2006). Moreover, it has been reported that increments of $[Na^+]_i$ of >5 mM may represent a critical threshold required to regulate NMDAR-mediated Ca^{2+} influx in primary cultures of hippocampal neurons (Xin et al., 2005). Consistent with these findings, the increment of $[Na^+]_i$ detected in immature cerebrocortical neurons seems to be sufficient to up-regulate NMDAR function.

Antillatoxin-Evoked Change in Membrane Potential Is Inadequate to Relieve the Mg^{2+} Blockade of NMDARs. Given the evidence in support of the involvement of NMDARs in ATX-induced stimulation of neuritogenesis, we considered mechanisms apart from the increment of $[Na^+]_i$. The ability of ATX to engage NMDARs could be a consequence of either the elevation of $[Na^+]_i$ or neuronal depolarization with attendant relief of the Mg^{2+} block of NMDAR. To ascertain the magnitude of ATX-induced membrane depolarization, we assessed membrane potential changes in DIV-1 cerebrocortical neurons by using the membrane-potential sensitive fluorescence dye, FMP blue.

As previously reported (George et al., 2009), FMP blue acted as a Nernstian fluorescent indicator of membrane potential in DIV-1 cerebrocortical neurons. This process was demonstrated by assessing the relationship between extracellular K^+ concentration and fluorescence intensity. Extracellular K^+ produced a concentration-dependent increase in maximal FMP blue fluorescence, consistent with a depolarization-induced redistribution of the lipophilic anion dye and attendant increase in fluorescence quantum efficiency (Fig. 7A). As depicted in Fig. 7B, the regression analysis for K^+ concentration-dependent changes in FMP blue fluorescence showed marked linear correlation (r^2 = 0.99). For a Nernstian fluorescent indicator of membrane potential, the ratio of fluorescence inside to the outside of the cell should be related to the membrane potential as described by the Nernst equation (Ehrenberg et al., 1988). This prediction is based on the principal that the membrane potential of isolated neurons is largely the result of the K^+ diffusion potential (Hille, 1992). Therefore, we used the Goldman-Hodgkin-Katz equation to generate a standard curve for the estimation of membrane potential (E_M) at various concentrations of extracellular K^+. The membrane potential of cerebrocortical neurons was dependent on the external concentration of K^+ (Hille, 1992). The concordance of the $[K^+]_{out}$ versus membrane fluorescence and $[K^+]_{out}$ versus E_M regressions indicates that changes in cerebrocortical neuron FMP blue fluorescence can be used to estimate membrane potential. Therefore, the re-

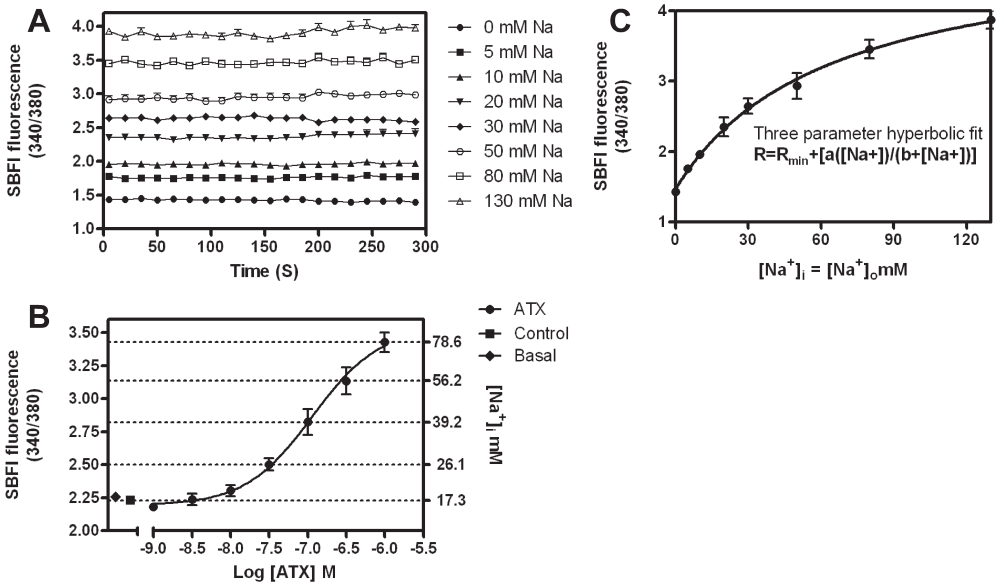

Fig. 6. Quantification of ATX-induced increase of intracellular sodium levels in DIV-1 cerebrocortical neurons. A, in situ calibration of SBFI fluorescence ratio (340/380). Time-response data show stepwise changes in SBFI fluorescence ratio values evoked by successive increments in extracellular sodium concentration. B, three-parameter hyperbolic fit adequately describes calibration data. C, nonlinear regression analysis of the ATX concentration-response data (EC_{50} = 114.2 nM; 70.8–184.1 nM 95% CI). Data represent the mean ± S.E.M. of two separate experiments each with 2 to 5 replicates. The scale on the left ordinate represents the SBFI fluorescence ratio, whereas that on the right ordinate depicts the $[Na^+]_i$ determined from the calibration curve shown in C. Addition of 30 nM ATX produced an 8.8-mM increment in $[Na^+]_i$ over basal.

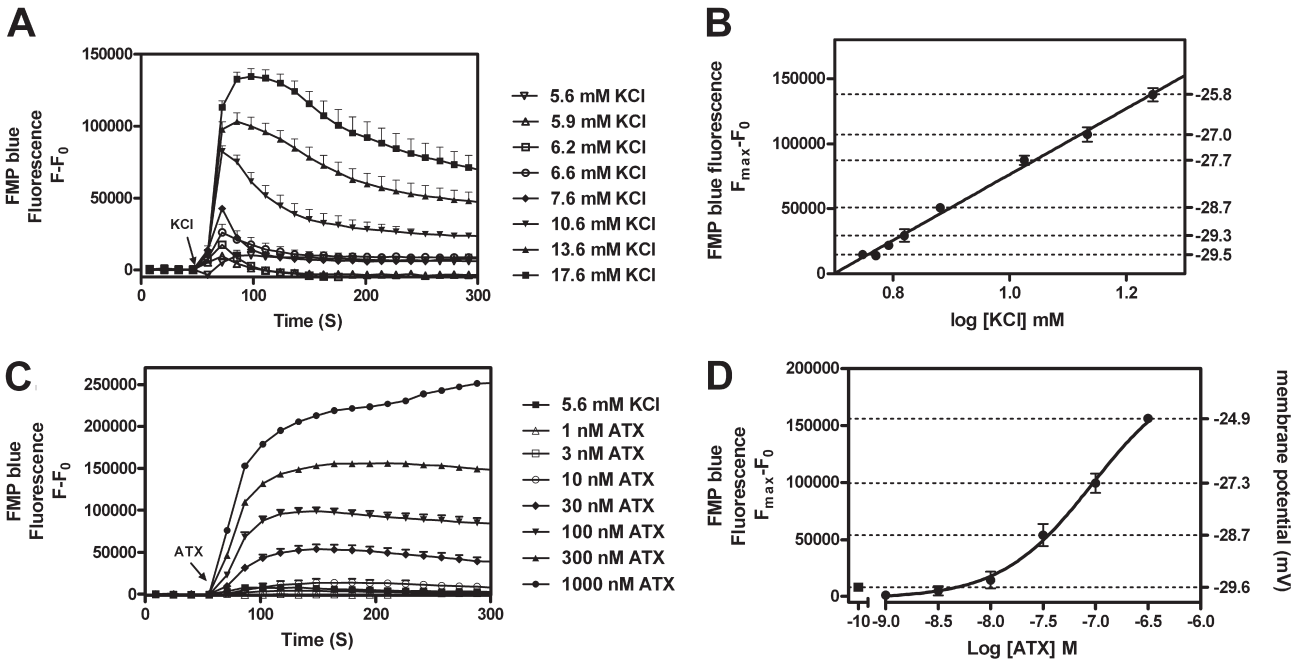

Fig. 7. ATX-evoked change in membrane potential in DIV-1 cerebrocortical neurons. A, concentration-response profile for KCl-evoked FMP blue fluorescence change as a function of time. Each point represents the mean ± S.E.M. of 3 to 9 values. B, the integrated time-response data for the increment in FMP blue fluorescence ($F_{max} - F_0$) plotted as a function of K^+ concentration. The displayed regression and correlation coefficient (r^2 = 0.995) were derived from linear regression analysis. The right ordinate scale shows membrane potential for each [K^+], which was calculated using the Goldman-Hodgkin-Katz equation as described under *Materials and Methods*. The resting membrane potential was −29.6 mV. C, time-response profiles for ATX-induced changes in membrane potential as determined by changes in FMP blue fluorescence. D, nonlinear regression analysis of the integrated time-response data for the increment in FMP blue fluorescence ($F_{max} - F_0$) as a function of ATX concentration. The membrane potential values were determined by performing K^+ calibration regressions in the same culture plate. The membrane potential change evoked by 30 nM ATX was 0.9 mV.

lationship between fluorescence change and E_M depicted in Fig. 7B was generated to determine ATX-induced changes in membrane potential of cerebrocortical neurons. The resting membrane potential of DIV-1 cerebrocortical neurons was found to be −29.6 mV. This result is consistent with previous demonstrations of a relatively depolarized resting membrane potential of immature neurons that later becomes more hyperpolarized as neurons mature (Ramoa and McCormick, 1994; Kim et al., 1995). As shown in Fig. 7C, ATX produced a rapid and concentration-dependent increment in FMP blue fluorescence in DIV-1 cerebrocortical neurons. Nonlinear regression analysis of the ATX concentration-response relationship yielded an EC_{50} value of 92.3 nM (63.6–136.8 nM, 95% CI) (Fig. 7D). Because the 30 nM concentration of ATX was sufficient to elevate $[Na^+]_i$, it was important to assess the membrane potential changes associated with this treatment. The 30 nM ATX treatment produced a transient increase in FMP blue fluorescence that was equivalent to the fluorescence change produced by an extracellular K^+ concentration of 7.6 mM. The corresponding membrane potential change was accordingly found to be negligible, representing only a 0.9 mV depolarization (from −29.6 ± 0.01 to 28.7 ± 0.15 mV). Therefore, this change in membrane potential would not be sufficient to influence the voltage-dependent Mg^{2+} block of NMDARs (Mayer et al., 1984).

A relatively depolarized resting membrane potential is recognized to be a characteristic of immature neurons that results, in part, from a high intracellular Cl^- concentration in embryonic neurons. We confirmed the resting membrane potential and influence of ATX (100 nM) on membrane potential in DIV-1 neurons by using noninvasive single-channel recordings (Tyzio et al., 2003). Measurement of single-channel NMDA receptor currents in cell-attached mode indicated that the resting membrane potential of DIV-1 neurons was −27.5 ± 3.65 mV, and 100 nM ATX shifted this by only 1.1 mV to a value of −26.4 ± 4.27 mV (Fig. 8). This approach provides an independent confirmation of the DIV-1 cerebrocortical neuron resting membrane potential determined with

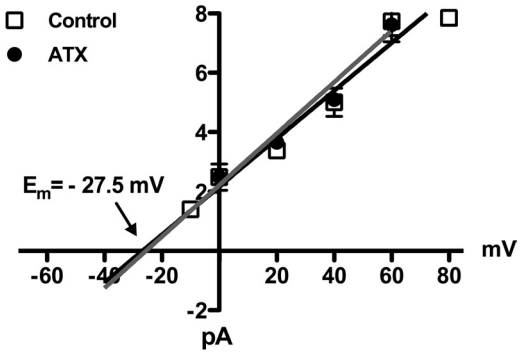

Fig. 8. Assessment of resting membrane potential of DIV-1 neurons and the effect of ATX on membrane potential was performed by using NMDA receptor cell-attached recordings as a voltage sensor. Current-voltage relationships of single-channel NMDA receptor currents were performed in a cell-attached mode. Under conditions where NMDA receptors exhibit linear current-voltage relationship and reverse at 0 mV, the expected membrane potential of the cell will be equal to the pipette potential at which the NMDA channel reverses in cell-attached mode. The currents through NMDA channels reversed at a pipette holding potential of −27.5 ± 3.65 mV. ATX (100 nM) application had a modest effect on the reversal potential of NMDA channels shifting it from −27.5 to −26.4 ± 4.27 mV. Each data point represents the mean ± S.E.M. of 4 to 6 recordings.

the Nernstian dye, FMP blue, and further supports our suggestion that the change in membrane potential produced by ATX is negligible and not sufficient to relieve Mg^{2+} block.

Antillatoxin Increases Intracellular Calcium Levels ($[Ca^{2+}]_i$) in DIV-1 Cerebrocortical Neurons. Previous studies have suggested that activity-dependent neuritogenesis and neuronal development involves Ca^{2+}-dependent signaling pathways through NMDAR and VGCCs. Due to the finding that ATX-induced neurite outgrowth involved NMDARs and VGCCs, we hypothesized that ATX exposure would produce Ca^{2+} influx in these immature cerebrocortical neurons. To investigate this theory, cells loaded with fluo-3 were exposed to various concentrations of ATX, and $[Ca^{2+}]_i$ was monitored. ATX produced rapid and concentration-dependent increases in $[Ca^{2+}]_i$, with even 30 nM ATX producing a significant increase in calcium influx (Fig. 9A).

To delineate the Ca^{2+} influx pathways triggered by ATX, the role of VGSCs, NMDARs, and VGCCs in DIV-1 cerebrocortical neurons was investigated. A pharmacologic evaluation of the $[Ca^{2+}]_i$ response to 100 nM ATX was performed. Cells were pretreated with specific antagonists—TTX (VGSCs), MK-801 (NMDARs), or nifedipine (VGCCs) to evaluate the role of these channels in ATX-induced Ca^{2+} influx. TTX (1 μM) completely blocked the response to ATX (data not shown), whereas MK-801 (1 μM) and nifedipine (1 μM) both significantly reduced ATX-induced Ca^{2+} influx (*, $p < 0.05$) (Fig. 9, B and C). Given the previously demonstrated role of SFK activation in the up-regulation of NMDAR function and in ATX-induced neurite outgrowth, we examined the role of SFKs in ATX-induced Ca^{2+} influx. PP2 (2 μM), a specific SFK family inhibitor, but not PP3 (2 μM), blocked ATX stimulation of Ca^{2+} influx consistent with the involvement of a SFK in this response (*, $p < 0.05$) (Fig. 9, D and E).

Antillatoxin Increases NMDA Receptor Single-Channel Open Probability but Not the Mean Open Time. To gain insight into the effect of ATX on single-channel properties of NMDA receptors, unitary currents were recorded from DIV-1 cerebrocortical neurons. Cell-attached patch recording was performed with 100 μM NMDA and 100 μM glycine in the patch pipette at a patch potential of +60 mV. Experiments were performed in the nominal absence of extracellular Mg^{2+} in the recording buffer supplemented with 20 μM

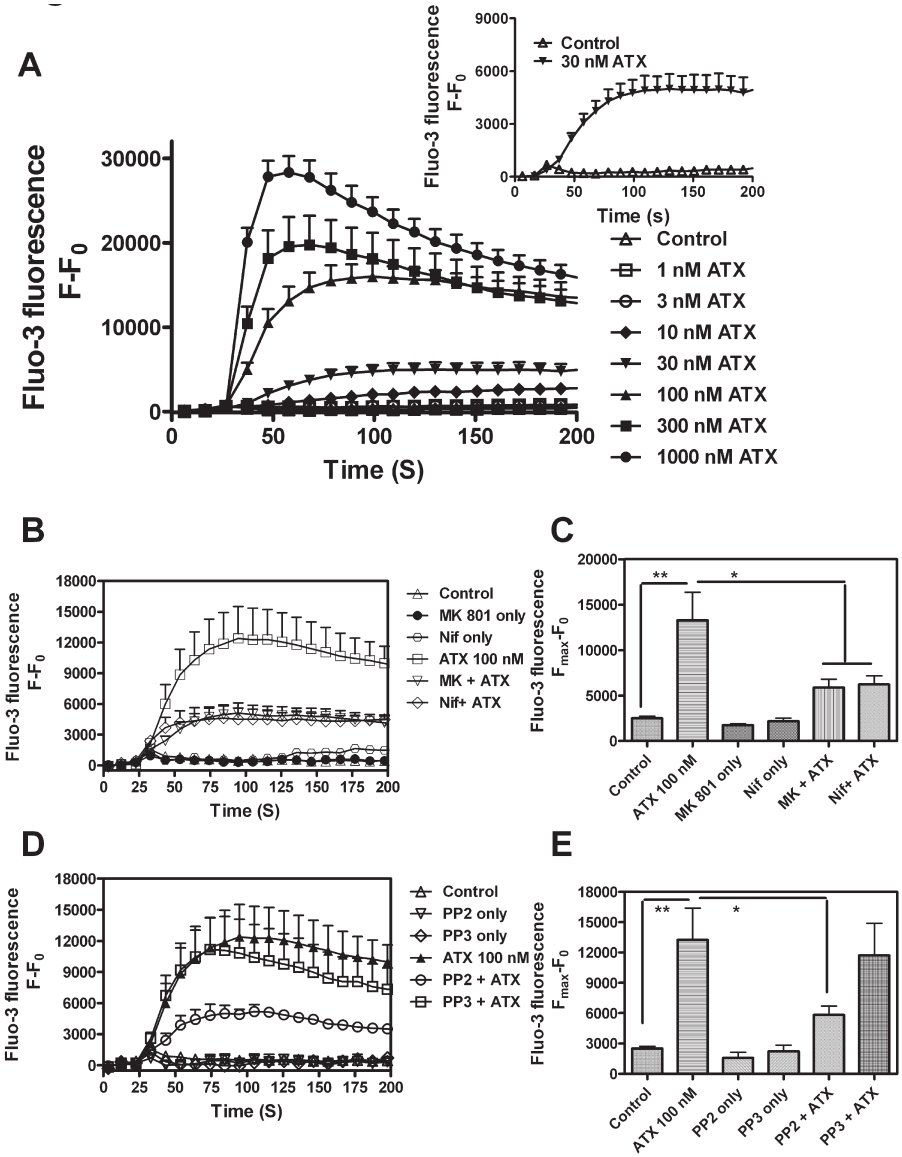

Fig. 9. ATX-induced Ca^{2+} influx and pharmacological evaluation in DIV-1 cerebrocortical neurons. A, time-response profile of ATX-induced Ca^{2+} influx in fluo-3-loaded cerebrocortical neurons. Data shown are from a representative experiment performed with 2 to 5 replicates per point and repeated twice. ATX (30 nM) produced a significant increase in Ca^{2+} influx in these DIV-1 cerebrocortical neurons (inset). B, pharmacological evaluation of ATX (100 nM) induced Ca^{2+} influx. Data are from a representative experiment performed in triplicate and repeated twice. Cerebrocortical neurons were treated with either 1 μM MK-801 or 1 μM nifedipine before the addition of 100 nM ATX. C, histogram representing quantification of the data shown in B. MK-801 and nifedipine significantly blocked ATX-induced calcium influx. D, involvement of Src family kinase in ATX-induced Ca^{2+} influx. Data are from a representative experiment performed in triplicate and repeated twice. Cerebrocortical neurons were treated with either 2 μM PP2 or 2 μM PP3 before the addition of 100 nM ATX. E, histogram representing quantification of the data shown in D. **, $p < 0.005$, *, $p < 0.05$, unpaired t test.

EDTA to chelate trace amounts of divalent ions. In the majority of patches, only single openings were observed with no apparent simultaneous double openings. The absence of double openings can presumably be attributed to the supposedly low expression of NMDA receptors in immature cerebrocortical neurons. Patches in which we observed simultaneous double openings were not further analyzed. Single-channel recordings were idealized using the QUB software and analyzed using ChanneLab with an imposed resolution of 50 μs. Bath application of 100 nM ATX significantly increased the P_o of NMDA receptors from 0.0053 ± 0.002 under control conditions to 0.012 ± 0.004 (206 ± 46% of control) after ATX ($n = 6$, $p < 0.05$, paired t test) (Fig. 10, A and B). The mean open time was not affected by ATX (1.862 ± 0.38 ms without ATX; 1.90 ± 0.38 ms, with ATX-101 ± 4.5% of control) ($n = 8$, $p < 0.05$, paired t test) (Fig. 10B). ATX similarly did not affect the amplitude of single-channel currents (data not shown). The composite open and shut dwell-time histograms were generated and fitted using Channelab. The open time histogram could be fitted by the sum of three exponential components with time constants of 0.127 (27%), 1.584 (53%), and 3.5 (20%). The time constants after ATX application were 0.091 (19%), 1.409 (70%), and 4.67 (11%). The composite shut time histograms could be fitted by sum of five exponential components with time constants of 0.7 (34%), 0.095 (17%), 20.8 (14%), 240 (22%), and 1090 (12%). The time constants were similar after ATX application 0.78 (35%), 0.169 (23%), 11.0 (10%), 84 (16%), and 580 (16%), except that the duration of the longer shut time constants were reduced (Fig. 10C).

Discussion

ATX is a novel activator of VGSC; however, its precise recognition site on the channel protein remains to be defined. The structure of ATX includes asymmetric carbon atoms, and the (4*R*,5*R*)-isomer is the naturally occurring compound. The (4*R*,5*R*)-isomer appears in profile as an "L" shape with a hydrophobic interior and a cluster of hydrophilic groups on the exterior of the macrocycle (Li et al., 2004). Thus, the (4*R*,5*R*)-configuration is important for creating a molecular topology that is recognized by the acceptor site on the voltage-gated sodium channel α subunit.

We have shown that ATX allosterically enhances the specific binding of [^{3}H]batrachotoxin to intact cerebellar granule cells (Li et al., 2001). This effect of ATX on [^{3}H]batrachotoxin binding was synergistically augmented by brevetoxin. The strong synergistic interaction of the ATX recognition site with neurotoxin site 5 suggests that these sites may be topologically close and/or conformationally coupled. The results obtained using [^{3}H]batrachotoxin as a probe for sodium channel conformation allowed us to exclude the interaction of ATX with neurotoxin sites 1, 2, 3, and 5 on VGSCs. Site 1 was ruled out because tetrodotoxin and saxitoxin bind to the outer vestibule of the pore of the ion channel and allosterically inhibit the binding of [^{3}H]batrachotoxin; this is an effect that is antipodal to that of ATX. We were able to rule out sites 2 and 5 inasmuch as these sites display positive allosteric coupling to the ATX site. Neurotoxin receptor site 3, the target for α-scorpion toxins and sea-anemone toxins, was excluded because ATX enhanced [^{3}H]batrachotoxin binding in the presence of a maximally effective concentration of sea-anemone toxin. Although we cannot exclude an interaction of ATX with neurotoxin site 4, the target for β-scorpion toxin, it is reasonable to posit that ATX binds to a novel recognition domain on the α-subunit of the VGSC. The relatively small lipotripeptide structure of ATX would not be restricted to an extracellular target, as is the case for the scorpion toxins, which are composed of 60 to 65 amino acids. Given the unique structure and mechanism of action of ATX, we sought to further characterize its pharmacologic actions in cerebrocortical neurons.

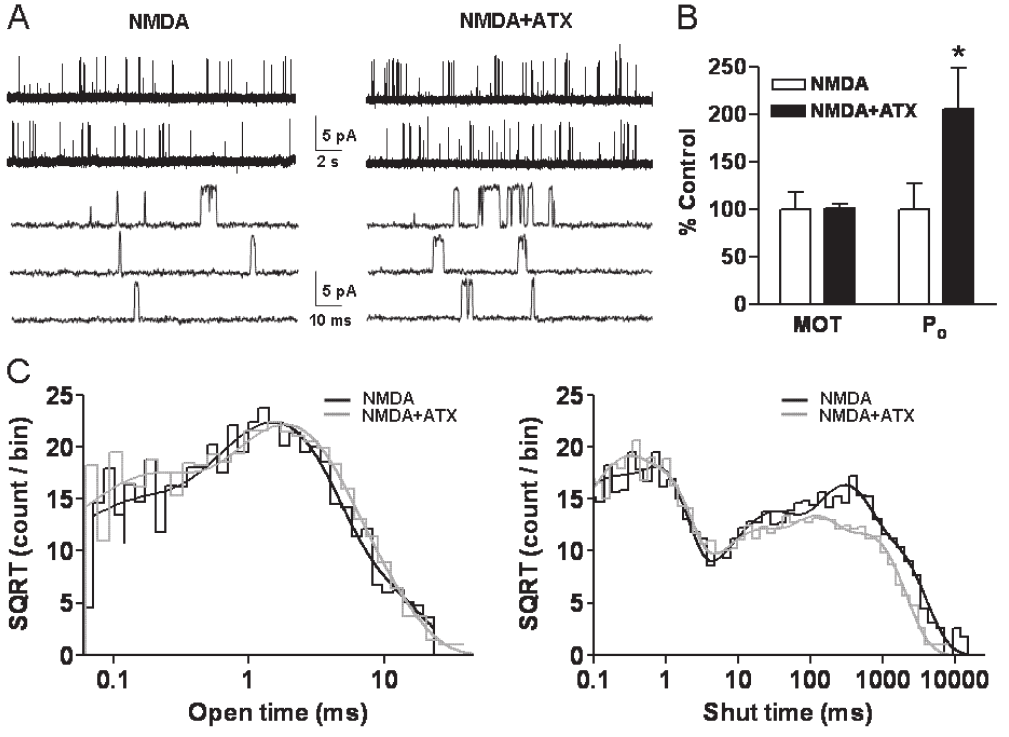

Fig. 10. Increase in NMDA receptor channel open probability by ATX. A, cell-attached patch recording from DIV-1 cerebrocortical neurons. NMDA receptor unitary currents were evoked by 100 μM NMDA and 100 μM glycine in the patch pipette (pipette potential = +60 mV, filtered at 5 kHz for representation, digitized at 40 kHz). Enhancement of NMDA receptor activity by bath application of 100 nM ATX. B, bath application of 100 nM ATX increased NMDA receptor channel P_o, but not the mean open time (MOT) ($n = 6$, *, $p < 0.05$, paired t test). C, pooled dwell-time histograms were fitted using Channelab. The open-time histogram was fitted by the sum of three Gaussian components, and the shut-time histogram was fitted by the sum of five Gaussian components. The time constants and area are described under *Results*.

We previously demonstrated that NMDA receptor function may be increased through activation of VGSCs with attendant elevation of intracellular sodium in cerebrocortical neurons (George et al., 2009). VGSC activators function as gating modifiers that elevate $[Na^+]_i$ in the absence of substantial depolarization of neurons (Cao et al., 2008; George et al., 2009). These findings have been confirmed and extended in the present study by demonstrating that the structurally novel lipopeptide, ATX, stimulates neuritogenesis in DIV-1 cerebrocortical neurons. These findings in DIV-1 murine cerebrocortical cultures provide compelling evidence in support of a role for $[Na^+]_i$ in activity-dependent processes of neuronal development.

Antillatoxin Enhances Neurite Outgrowth. In this study, we found that ATX enhanced neurite outgrowth in DIV-1 cerebrocortical neurons as a result of elevation of cytoplasmic $[Na^+]$, potentiation of NMDAR function, and stimulation of calcium influx. ATX enhanced total neurite outgrowth in immature cerebrocortical neurons in a bidirectional, or hormetic, concentration-response relationship, with 30 to 100 nM producing robust increases of more than 2-fold (Fig. 2). Thus, the ability of ATX to augment NMDAR channel activity translated into an enhancement of the trophic influence of NMDAR on developing cerebrocortical neurons. Based on the premise that the effects of neuronal activity on dendritic arbor growth and structural plasticity are primarily mediated by engagement of NMDA receptors (Tolias et al., 2005), our results suggest that ATX activation of sodium channels with attendant enhancement of NMDA receptor signaling mimics the response to neuronal activity.

Antillatoxin Concentration Response for Neurite Growth Is an Inverted U. An inverted-U model describes the relationship between NMDA receptor activity and neuronal survival and growth (Lipton and Nakanishi, 1999). This inverted-U concentration-response relationship has primarily, but not exclusively, been attributed to $[Ca^{2+}]_i$ regulation. An optimal window for $[Ca^{2+}]_i$ is required for activity-dependent neurite extension and branching, with lower levels stabilizing growth cones and higher levels stalling them, in both cases preventing extension (Gomez and Spitzer, 2000; Hui et al., 2007). Although the precise mechanism for the ATX bidirectional concentration-response curve is not known, one plausible explanation therefore is related to the involvement of NMDA receptors in the trophic response to ATX. Other potential explanations for the inverted U response include the possibility that high concentrations of ATX might promote slow inactivation of VGSCs with attendant reduction in sodium influx (Mitrovic et al., 2000). Alternatively, high concentrations of ATX could increase VGSC internalization, which has been shown to be a consequence of Na^+ influx in immature neuronal tissue. These results with ATX concur with those recently reported for PbTx-2-induced stimulation of neuritogenesis in DIV-2 cerebrocortical neurons (George et al., 2009). Although PbTx-2 is known to activate neurotoxin site 5 on VGSC α-subunits, the molecular determinants for ATX on the VGSC remain to be defined (Li et al., 2001).

ATX stimulated Ca^{2+} influx in cerebrocortical neurons through both NMDARs and VGCCs. Ca^{2+}-signaling pathways initiated by Ca^{2+} entry through L-type Ca^{2+} channels and NMDA receptors have been shown to be different (Bading et al., 1993). Although MK-801 and nifedipine produced comparable reductions in ATX-induced Ca^{2+} influx, we found that the NMDAR antagonist MK-801 completely blocked ATX-enhanced neurite outgrowth, whereas the L-type calcium channel blocker nifedipine produced only a partial block of the stimulation of neurite outgrowth. These results suggest that Ca^{2+}, which enters neurons through NMDA receptors, may have privileged access to the CaMKK and CaMKI signaling elements that drive neuritogenesis.

In mature neurons, a strong depolarizing stimulus (50 mM KCl) is required for the engagement of L-type Ca^{2+} channels in dendritic growth and arborization, whereas a smaller depolarizing stimulus (16 mM KCl) induced neurite outgrowth preferentially due to Ca^{2+} influx through NMDARs (Redmond et al., 2002; Wayman et al., 2006). Our observation that ATX concentrations of 30 to 100 nM provided a sufficient stimulus to produce Ca^{2+} influx through VGCCs may be explained by the relatively depolarized resting membrane potential of immature cerebrocortical neurons. The resting membrane potential of DIV-1 cerebrocortical neurons was found to be -29.6 mV, and ATX (30–300 nM) produced modest changes of 1 to 5 mV. However, these modest changes in membrane potential produced by ATX may be sufficient to activate L-type Ca^{2+} channels given the relatively depolarized resting membrane potential (Nowycky et al., 1985).

Regulatory Influence of Na^+ on NMDAR Activity. Recent studies have shown that intracellular Na^+ might act as a signaling molecule. Based on the original work of Hodgkin and Huxley (1952) with squid axons, a single action potential was calculated to minimally change the Na^+ electrochemical gradient (Hille, 1992). However, the situation in mammalian neurons with fine axons, dendrites, and spines is much different due to greater surface-to-volume ratios. Thus, a single action potential may elevate $[Na^+]_i$ substantially (Hille, 1992). Yu et al. (1997) and Yu and Salter (1998) previously demonstrated that elevation of intracellular Na^+ increases NMDA receptor-mediated whole-cell currents and NMDAR single-channel current by increasing the open probability and mean open time of the channel. An increment of $[Na^+]_i$ of 10 mM was sufficient to produce significant increases in NMDA receptor single-channel activity. They used veratridine, a VGSC modulator, to demonstrate that Na^+ influx through TTX-sensitive VGSC was sufficient to upregulate NMDAR activity. Moreover, this Na^+-dependent regulation of NMDA receptor function was shown to be controlled by Src-induced phosphorylation of the receptor (Yu et al., 1997). These results were extended in the present study using the novel sodium channel activator ATX as a probe to elevate intracellular Na^+. Single-channel current recording in presence of ATX directly demonstrated the enhancement of NMDA receptor function. An increase in intracellular Na^+ and Src activation after exposure to ATX increased the open probability of the NMDAR. The shut time histogram with slow time constants resemble NR2B-containing receptors (Erreger et al., 2005), consistent with the expression of NR1/NR2B-containing receptors in immature neurons (Williams et al., 1993). Given that the single-channel recordings were done in the absence of extracellular Mg^{2+}, these results additionally argue against relief of the voltage-dependent Mg^{2+} block of the NMDAR in the actions of ATX. Therefore, these data confirm the regulatory influence of Na^+ on NMDAR channel activity in hippocampal neurons described previously (Yu and Salter, 1998) and extend this relationship

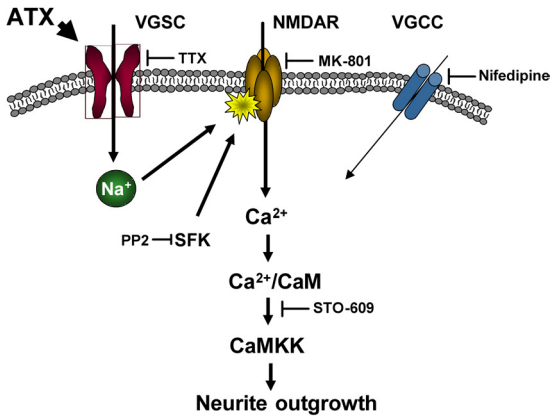

Fig. 11. Schematic diagram of the pathways involved in ATX-induced neurite outgrowth.

between $[Na^+]_i$ and NMDA receptor function to cerebrocortical neurons.

ATX represents a structurally and mechanistically novel activator of VGSCs whose recognition domain on the α-subunit remains to be established (Li et al., 2001). In this study, we found that ATX was capable of mimicking activity-dependent neuronal development by up-regulating NMDAR function. We propose a model for ATX-induced neuritogenesis (Fig. 11) that involves direct activation of TTX-sensitive VGSCs, elevation of $[Na^+]_i$, activation of a Src family kinase, potentiation of NMDAR function leading to Ca^{2+} influx, and engagement of a CaMKK pathway. We have recently reported that another activator of VGSCs, brevetoxin 2, is capable of up-regulating NMDAR function and stimulating neuritogenesis (George et al., 2009). Therefore, structurally dissimilar sodium channel activators seem to be capable of mimicking activity-dependent structural plasticity by up-regulating NMDA receptor signaling pathways.

References

Bading H, Ginty DD, and Greenberg ME (1993) Regulation of gene expression in hippocampal neurons by distinct calcium signaling pathways. *Science* **260:**181–186.

Bradford MM (1976) A rapid and sensitive method for the quantitation of microgram quantities of protein utilizing the principle of protein-dye binding. *Anal Biochem* **72:**248–254.

Cao Z, George J, Gerwick WH, Baden DG, Rainier JD, and Murray TF (2008) Influence of lipid-soluble gating modifier toxins on sodium influx in neocortical neurons. *J Pharmacol Exp Ther* **326:**604–613.

Ehrenberg B, Montana V, Wei MD, Wuskell JP, and Loew LM (1988) Membrane potential can be determined in individual cells from the nernstian distribution of cationic dyes. *Biophys J* **53:**785–794.

Erreger K, Dravid SM, Banke TG, Wyllie DJ, and Traynelis SF (2005) Subunit-specific gating controls rat NR1/NR2A and NR1/NR2B NMDA channel kinetics and synaptic signalling profiles. *J Physiol* **563:**345–358.

George J, Dravid SM, Prakash A, Xie J, Peterson J, Jabba SV, Baden DG, and Murray TF (2009) Sodium channel activation augments NMDA receptor function and promotes neurite outgrowth in immature cerebrocortical neurons. *J Neurosci* **29:**3288–3301.

Ghosh A and Greenberg ME (1995) Calcium signaling in neurons: molecular mechanisms and cellular consequences. *Science* **268:**239–247.

Gomez TM and Spitzer NC (2000) Regulation of growth cone behavior by calcium: new dynamics to earlier perspectives. *J Neurobiol* **44:**174–183.

Hille B (1992) Ionic channels of excitable membranes, in (Anonymous), Sinauer Associates, Sunderland, MA.pp 403–411.

Hodgkin AL and Huxley AF (1952) Currents carried by sodium and potassium ions through the membrane of the giant axon of Loligo. *J Physiol* **116:**449–472.

Hui K, Fei GH, Saab BJ, Su J, Roder JC, and Feng ZP (2007) Neuronal calcium sensor-1 modulation of optimal calcium level for neurite outgrowth. *Development* **134:**4479–4489.

Kim HG, Fox K, and Connors BW (1995) Properties of excitatory synaptic events in neurons of primary somatosensory cortex of neonatal rats. *Cereb Cortex* **5:**148–157.

Konur S and Ghosh A (2005) Calcium signaling and the control of dendritic development. *Neuron* **46:**401–405.

Lee KC and Loh TP (2006) Total synthesis of antillatoxin. *Chem Commun (Camb)* **40:**4209–4211.

Li WI, Berman FW, Okino T, Yokokawa F, Shioiri T, Gerwick WH, and Murray TF (2001) Antillatoxin is a marine cyanobacterial toxin that potently activates voltage-gated sodium channels. *Proc Natl Acad Sci U S A* **98:**7599–7604.

Li WI, Marquez BL, Okino T, Yokokawa F, Shioiri T, Gerwick WH, and Murray TF (2004) Characterization of the preferred stereochemistry for the neuropharmacologic actions of antillatoxin. *J Nat Prod* **67:**559–568.

Linden DJ, Smeyne M, and Connor JA (1993) Induction of cerebellar long-term depression in culture requires postsynaptic action of sodium ions. *Neuron* **11:**1093–1100.

Lipton SA and Nakanishi N (1999) Shakespeare in love–with NMDA receptors? *Nat Med* **5:**270–271.

Mayer ML, Westbrook GL, and Guthrie PB (1984) Voltage-dependent block by Mg2+ of NMDA responses in spinal cord neurones. *Nature* **309:**261–263.

Miller FD and Kaplan DR (2003) Signaling mechanisms underlying dendrite formation. *Curr Opin Neurobiol* **13:**391–398.

Mitrovic N, George AL Jr, and Horn R (2000) Role of domain 4 in sodium channel slow inactivation. *J Gen Physiol* **115:**707–718.

Nowycky MC, Fox AP, and Tsien RW (1985) Three types of neuronal calcium channel with different calcium agonist sensitivity. *Nature* **316:**440–443.

O'Brien JA and Lummis SC (2006) Diolistic labeling of neuronal cultures and intact tissue using a hand-held gene gun. *Nat Protoc* **1:**1517–1521.

Orjala J, Nagle D, Hsu V, and Gerwick WH (1995) Antillatoxin: an exceptionally ichthyotoxic cyclic lipopeptide from the tropical cyanobacterium lyngbya majuscula. *J Am Chem Soc* **117:**8281–8282.

Ramoa AS and McCormick DA (1994) Developmental changes in electrophysiological properties of LGNd neurons during reorganization of retinogeniculate connections. *J Neurosci* **14:**2089–2097.

Redmond L, Kashani AH, and Ghosh A (2002) Calcium regulation of dendritic growth via CaM kinase IV and CREB-mediated transcription. *Neuron* **34:**999–1010.

Rose CR and Konnerth A (2001) NMDA receptor-mediated Na+ signals in spines and dendrites. *J Neurosci* **21:**4207–4214.

Salter MW and Kalia LV (2004) Src kinases: a hub for NMDA receptor regulation. *Nat Rev Neurosci* **5:**317–328.

Saneyoshi T, Wayman G, Fortin D, Davare M, Hoshi N, Nozaki N, Natsume T, and Soderling TR (2008) Activity-dependent synaptogenesis: regulation by a CaM-kinase kinase/CaM-kinase I/betaPIX signaling complex. *Neuron* **57:**94–107.

Tolias KF, Bikoff JB, Burette A, Paradis S, Harrar D, Tavazoie S, Weinberg RJ, and Greenberg ME (2005) The Rac1-GEF Tiam1 couples the NMDA receptor to the activity-dependent development of dendritic arbors and spines. *Neuron* **45:**525–538.

Tyzio R, Ivanov A, Bernard C, Holmes GL, Ben-Ari Y, and Khazipov R (2003) Membrane potential of CA3 hippocampal pyramidal cells during postnatal development. *J Neurophysiol* **90:**2964–2972.

Ultanir SK, Kim JE, Hall BJ, Deerinck T, Ellisman M, and Ghosh A (2007) Regulation of spine morphology and spine density by NMDA receptor signaling in vivo. *Proc Natl Acad Sci U S A* **104:**19553–19558.

Wayman GA, Impey S, Marks D, Saneyoshi T, Grant WF, Derkach V, and Soderling TR (2006) Activity-dependent dendritic arborization mediated by CaM-kinase I activation and enhanced CREB-dependent transcription of Wnt-2. *Neuron* **50:**897–909.

West AE, Griffith EC, and Greenberg ME (2002) Regulation of transcription factors by neuronal activity. *Nat Rev Neurosci* **3:**921–931.

Williams K, Russell SL, Shen YM, and Molinoff PB (1993) Developmental switch in the expression of NMDA receptors occurs in vivo and in vitro. *Neuron* **10:**267–278.

Wong RO and Ghosh A (2002) Activity-dependent regulation of dendritic growth and patterning. *Nat Rev Neurosci* **3:**803–812.

Xin WK, Kwan CL, Zhao XH, Xu J, Ellen RP, McCulloch CA, and Yu XM (2005) A functional interaction of sodium and calcium in the regulation of NMDA receptor activity by remote NMDA receptors. *J Neurosci* **25:**139–148.

Yan X, Benson JM, Gomez AP, Baden DG, and Murray TF (2006) Brevetoxin-induced neural insult in the retrosplenial cortex of mouse brain. *Inhal Toxicol* **18:**1109–1116.

Yu XM (2006) The role of intracellular sodium in the regulation of NMDA-receptor-mediated channel activity and toxicity. *Mol Neurobiol* **33:**63–80.

Yu XM, Askalan R, Keil GJ 2nd, and Salter MW (1997) NMDA channel regulation by channel-associated protein tyrosine kinase Src. *Science* **275:**674–678.

Yu XM and Salter MW (1998) Gain control of NMDA-receptor currents by intracellular sodium. *Nature* **396:**469–474.

Address correspondence to: Dr. Thomas F. Murray, Creighton University School of Medicine, Department of Pharmacology, Omaha, NE 68178. E-mail: tfmurray@creighton.edu